Nonlinear Coded Nonuniform Superposed QAM by Trellis-coding for MISO System in Visible Light Communication

Zengyi Xu (徐增熠)[1, 2], Wenqing Niu (牛文清)[1], Jianyang Shi (施剑阳)[1], and Nan Chi (迟楠)[1*]

1Key Laboratory for Information Science of Electromagnetic Waves (MoE), Department of Communication Science and Engineering, Fudan University, Shanghai 200433, China, China;

2Peng Cheng Laboratory, Shenzhen 518055, China

*corresponding author: Nan Chi, Email：nanchi@fudan.edu.cn

Received Month X, XXXX; accepted Month X, XXXX; posted online Month X, XXXX

In this paper, we propose a 36-QAM superposition modulation technique that featured with uneven symbol probability by nonlinear precoding, named Nonlinear Coded Nonuniform Superposition QAM (NCNS-QAM). Its aim is to alleviate the nonlinearity effect caused by high instantaneous power in multi-input-single-output (MISO) visible light communication system (VLC), with an uneven probabilistic-shaped constellation. The transmitter includes two LEDs to send signal independently, and the receiver uses a PD to receive the superposed QAM signal. The experiment results show that NCNS has a better robustness against nonlinearity than PAM4, approximately gaining a 16% increase in maximum usable peak-to-peak voltage and a 33% enlargement in dynamic range area. It is a simple but effective approach to solve the bandwidth limits related to signal power and hopefully could be applied in large power VLC system such as underwater VLC (UVLC), or improve the robustness against power fluctuation.

***Keywords**: VLC, LED, MISO, QAM, nonlinear coding, spectral shaping*
DOI: 10.3788/COL202220.042501

1. Introduction

Visible light communication (VLC) system, which utilizes the 400-800 THz spectrum, is predicted as a promising technique in the upcoming 6G communication, due to its desired characteristics such as high confidentiality, rich spectrum resources, free from license and patent, low electromagnetic pollution and other advantages [1].

Multi-input multi-output (MIMO) system has proven its importance in the past 4G and current 5G network [2]. It solves the demanding challenge for communication capacity and provides large-scale access for massive users. It's single-output version is termed MISO. It is believed that this technology would continue to play a crucial role in 6G to implement a more massive connectivity [3],[4], which paves the way to an 'Internet of Everything' (IoE) network.

This situation encourages the combination of VLC with MIMO/MISO, where LED and photo detector (PD) arrays resembles the antennas in their RF counterparts. The bandwidth limitation of LED can be compensated by increasing the number of parallel transmitters [5]. Meanwhile, compared with RF system, it has a potential to be integrated into indoor illuminating system. Existing works [6]-[9]has explored the application of MIMO/MISO in VLC system. A common point in these works is that independent signals are superposed at the same receiver.

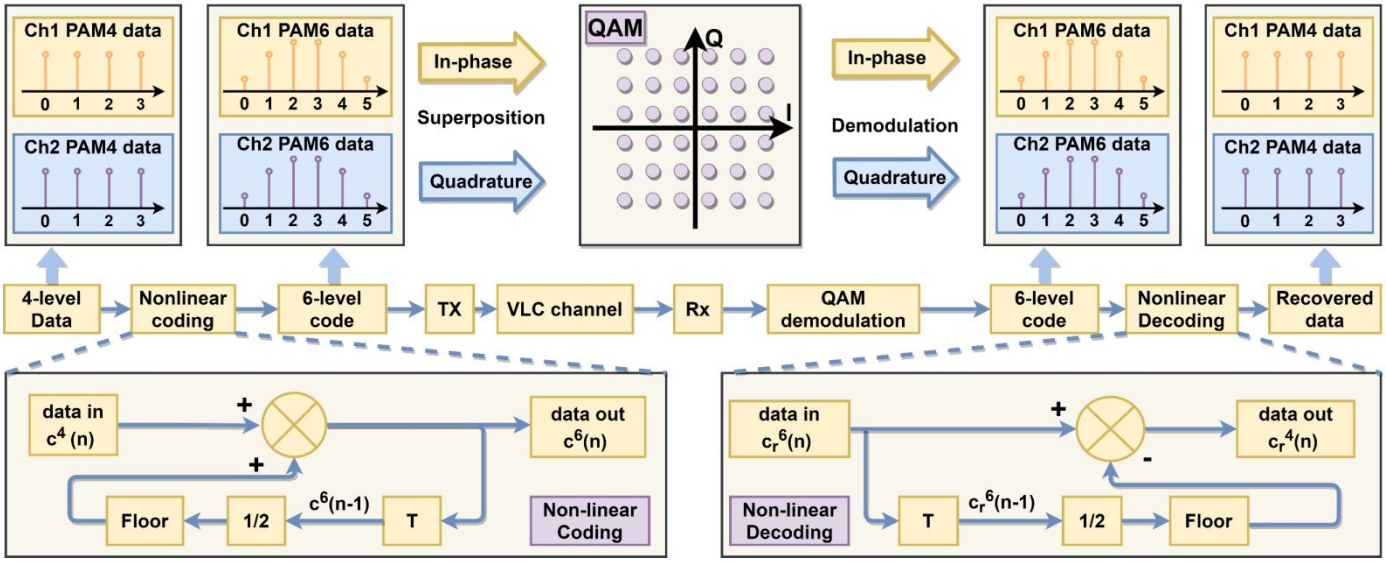

Figure 1. The principle of NCNS-QAM algorithm, a 36 QAM is implemented by superposing two independent PAM6 signals generated by the original PAM4 ones. The in-phase and quadrature signals are later demodulated as in regular QAM scheme, resulting in two independent PAM6 data. After the nonlinear decoding step, the original PAM4 data is recovered.

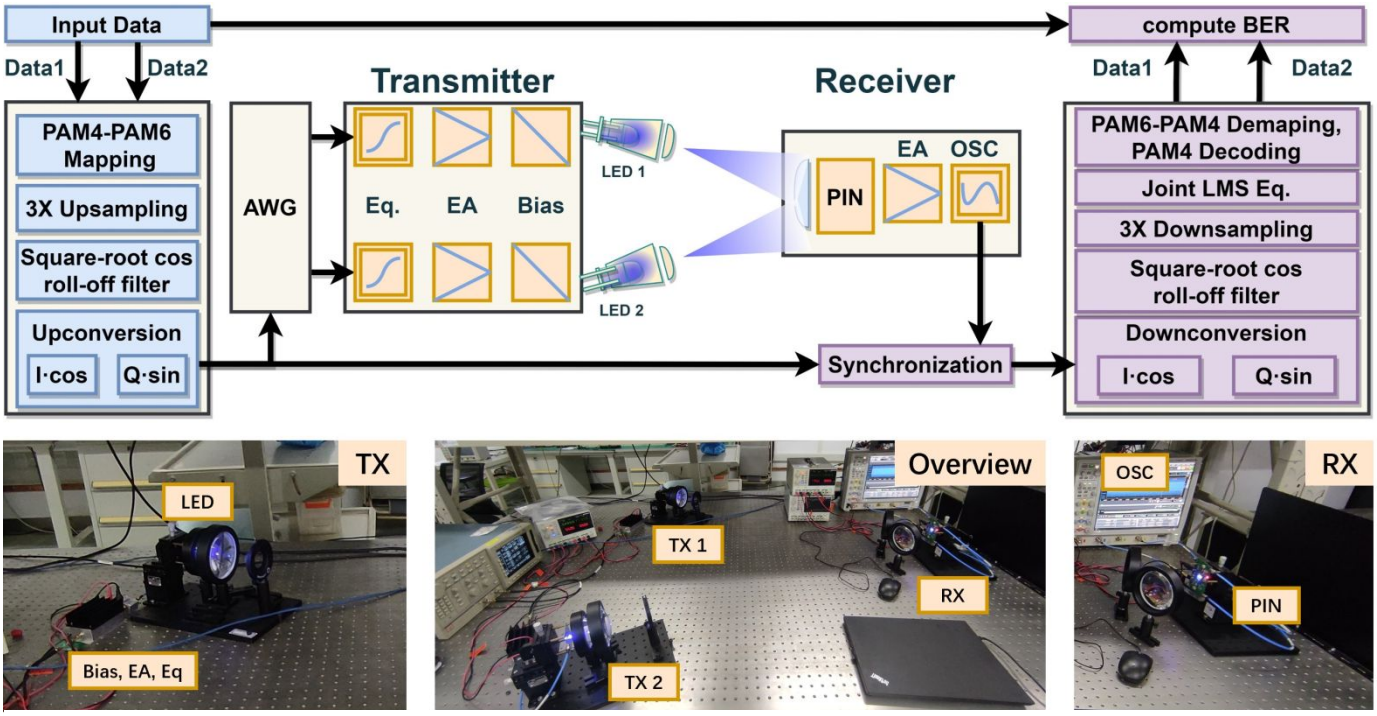

Figure 2. The setup for the NCNS-QAM experiment. Two independent LED channels transmit optical signal which is received by a single PIN detector. The original 4-level PAM4 signal experiences nonlinear coding (PAM4 to 6 mapping), upsampling, roll-off filtering, before upconversion. In upconversion, the two channels are mixed with orthogonal carriers and thus forms a QAM signal at the receiver. After the signal is received, it undergoes downconversion (as in QAM demodulation), roll-off filtering, joint LMS equalization and nonlinear decoding. TX: transmitter, Rx: receiver, Eq.: hardware equalizer, EA: electrical amplifier, OSC: oscilloscope, PIN: p-i-n photodetector

However, the nonlinearity effect is a severe issue in VLC [10] . Apart from the nonlinearity from the LED transmitter, the instantaneous photo voltage on PD at the receiver is more likely to enter the nonlinear region due to the multi-fold incident light power. The degraded response characteristic deteriorates the communication quality and raise the bit error rate (BER) above the threshold for forward error correction (FEC).

Nonlinear coding is an effective measure to alleviate the negative influence from nonlinearity, which is able to modify the signal in either time domain or frequency domain (or both), in the meantime. As some of them applies trellis-coded modulation (TCM) that adds correlation between adjacent symbols [13]-[16]. Thus, their symbols appear in a nonuniform probability distribution. In this paper, we are inspired by Yamamoto et al in [17],[18], where they present a Trellis-coded nonlinear precoding technique, which also changes the probability distribution. But unlike probabilistic shaping (PS), it does not require a distribution matcher (DM) or add redundancy in the transmitted sequence [19]. Meanwhile, its spectrum shows a prominent mid-frequency band. Compared with precoding using Tomlinson-Harashima precoding (THP), this algorithm consumes significantly less computation because it does not perform an estimation using previous symbols [20].

However, the previous work in [17] and [18] separates the transmission of two different channels using two independent receivers. With scalar superposed coded modulation (Scalar-SCM), it could form a superposed QAM signal at the receiver, which follows similar demodulation purpose but has an unevenly distributed constellation point. Instead of using unbalanced coding schemes for different channels [21], the two channel uses identical process of precoding. In this paper, we explored this application in MISO VLC system and named it nonlinear-coded nonuniform superposition QAM (NCNS-QAM).

Joint LMS (MIMO LMS) software equalizer [22] is utilized to compensate inter-symbol interference (ISI) and inter-channel interference (ICI), by deducting the product of the symbol value and the tap weights from the received signal. Because it only concerns with the input, it also suits MISO systems. In this experiment, its tap weights also provide insights for the ISI and ICI.

2. Methodology

Applying the algorithm shown in Figure 1, which is described by Yamamoto et al in [17],[18], two independent 6-level code $c^6(n)$is obtained from two uniformly distributed 4-level signal $c^4(n)$. It leaves a clear path in the Trellis diagram. The distribution of $c^6(n)$ can be written in the following form:

$$\boldsymbol{P} = [P_0, P_1, P_2, P_3, P_4, P_5]^T = \left[\frac{1}{16}, \frac{3}{16}, \frac{4}{16}, \frac{4}{16}, \frac{3}{16}, \frac{1}{16}\right]^T \# \quad (1)$$

, which is the eigenvector corresponding to the unity eigenvalue of the transition matrix. Two independent channels would result in a 2D constellation with nonuniform distribution of probability:

$$P_X = \boldsymbol{P}\boldsymbol{P}^T = \begin{bmatrix} \frac{1}{256} & \frac{3}{256} & \frac{4}{256} & \frac{4}{256} & \frac{3}{256} & \frac{1}{256} \\ \frac{3}{256} & \frac{9}{256} & \frac{12}{256} & \frac{12}{256} & \frac{9}{256} & \frac{3}{256} \\ \frac{4}{256} & \frac{12}{256} & \frac{16}{256} & \frac{16}{256} & \frac{12}{256} & \frac{4}{256} \\ \frac{4}{256} & \frac{12}{256} & \frac{16}{256} & \frac{16}{256} & \frac{12}{256} & \frac{4}{256} \\ \frac{3}{256} & \frac{9}{256} & \frac{12}{256} & \frac{12}{256} & \frac{9}{256} & \frac{3}{256} \\ \frac{1}{256} & \frac{3}{256} & \frac{4}{256} & \frac{4}{256} & \frac{3}{256} & \frac{1}{256} \end{bmatrix} \# \quad (2)$$

, where P_X is the probability matrix of the combined vector symbol at the receiver. $P_{X_{ij}} = P_i \cdot P_j$, $X_{i,j}$ represent the case when channel 1 transmits the i^{th} 6-level signal and channel 2 transmits the j^{th}.

To implement the vector symbol in a MISO system, firstly, the positive integers in $c^6(n)$ are shifted and scaled into $c'^6(n) \in \{-5, -3, -1, 1, 3, 5\}$ as PAM modulation requires. It needs upsampling and roll-off filtering process to achieve pulse shaping.

$$\begin{bmatrix} c_1(t) \\ c_2(t) \end{bmatrix} = \begin{bmatrix} g(t) \otimes c_1^{up}(t) \\ g(t) \otimes c_2^{up}(t) \end{bmatrix} \#(3)$$

, where $c^{up}(t)$ is the upsampled 6-level code from $c'^6(n)$, and $c(t)$ is the result from the filter.

Next, the filtered samples are mixed with one of the two orthogonal carriers, either $\sin 2\pi f_0 t$ or $\cos 2\pi f_0 t$ as the equation describes:

$$\begin{cases} PAM_1(t) = c_1'(n) \cdot \cos 2\pi f_0 t \\ PAM_2(t) = c_2'(n) \cdot \sin 2\pi f_0 t \end{cases} \# \quad (4)$$

The expression for the two PAM signals reminds us the description of the in-phase and quadrature component in QAM. One pair of superposed orthogonal signals can be regarded as a single complexed valued QAM symbol:

$$sQAM(t) = PAM_1(t) + j\,PAM_2(t) \#(5)$$

, which can be written in complex-valued expression:

$$s\,QAM(t) = \boldsymbol{X}(n) \cdot e^{j(2\pi f_0 t)} \#(6)$$

where $\boldsymbol{X}(n) = c_1'(n) + jc_2'(n)$. Thus, the input scalar symbol is already converted into a vector symbol. However, the probability of each symbol is not equal due to the uneven distribution of $c'(t)$. To decode the 36 QAM signal, the process is similar to that in QAM.

$$\begin{bmatrix} R_1(t) \\ R_2(t) \end{bmatrix} = \begin{bmatrix} \cos(2\pi f_0 t) & 0 \\ 0 & -\sin(2\pi f_0 t) \end{bmatrix} \begin{bmatrix} sQAM(t) \\ sQAM(t) \end{bmatrix} \#(7)$$

The result experiences down sampling and another round of roll-off filtering with the same parameter as in (3) to obtain the recovered data R_{rec1} and R_{rec2}.

$$\begin{bmatrix} R_{rec2}(t) \\ R_{rec1}(t) \end{bmatrix} = \begin{bmatrix} g(t) \otimes R_1^{down}(t) \\ g(t) \otimes R_2^{down}(t) \end{bmatrix} \#(8)$$

The recovered data is later processed using maximum likelihood decision (or minimum Euclidian distance). The result is 6-level code $c_{r1}^6(n)$ and $c_{r2}^6(n)$. By applying the nonlinear decoding algorithm illustrated in Figure 1, a 4-level recovered data would be obtained.

This precoding technique has a linear time complexity O(n-1) to the length n of the original 4-level code and a fixed space complexity O(1) as the memory only stores the last 6-level code and the current 4-level one to encode a new 6-level one.

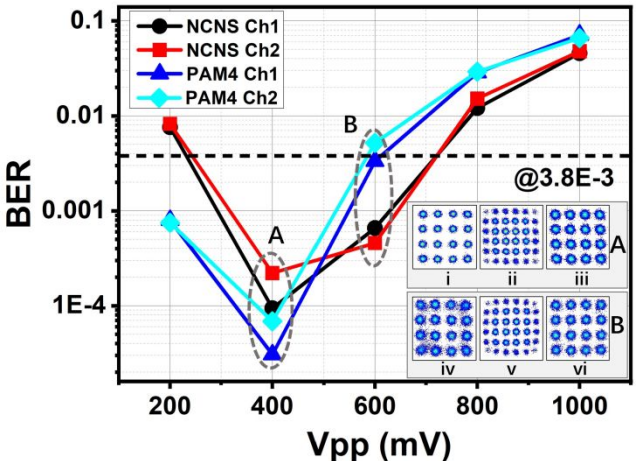

Figure 3. BER versus Vpp for both PAM4 and NCNS. The A group insets are the constellation diagrams at 400 mV: (i) PAM4 (ii) NCNS (iii) the 4-level decoded result from NCNS. The B group insets are the constellation diagrams at 600 mV: (iv) PAM4 (v) NCNS (vi) the 4-level decoded result from NCNS.

The experiment setup is illustrated in Figure 2. The input data is firstly encoded into PAM4 and afterwards mapped into PAM6. The signal is upsampled by three times and experiences a square-root cosine roll-off filter to control its spread in time-domain. The up-conversion step divides the signal into an in-phase and

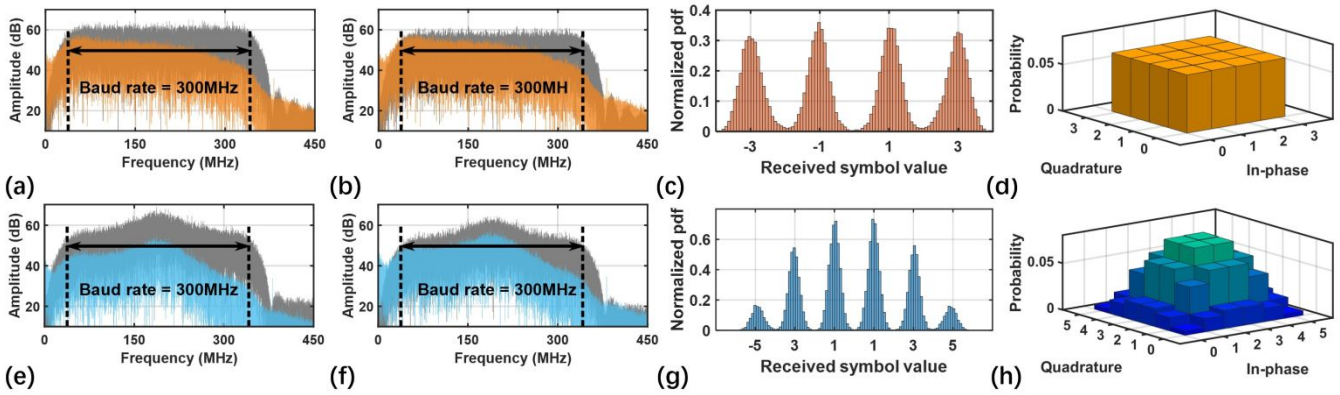

Figure 4. The first and second column are the spectra of TX and RX signal in both PAM4 (orange) and NCNS (blue). (a), (e) Vpp=400mV, (b), (f) Vpp=600mV. The third column is the probability density of RX symbol under 600mV in (c) PAM4, (g) NCNS. The last column is the probability distribution of each symbol in superposed QAM by (d) PAM4 or (h) NCNS when transmitting the same length of original data.

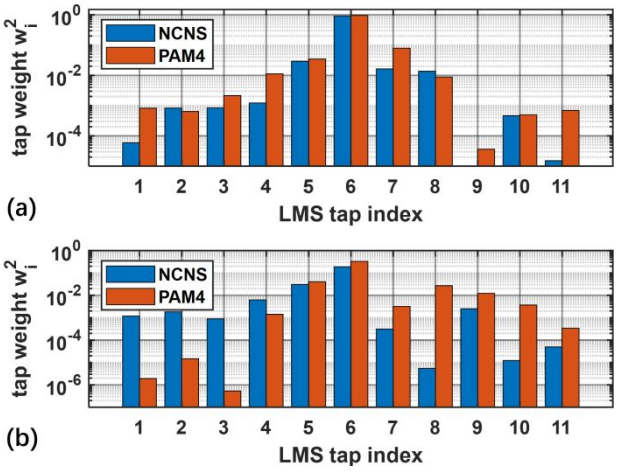

Figure 6. The joint LMS equalizer tap weights in channel 1. (a) shows the tap weights w_{11} for compensating inter-symbol interference (ISI) from channel 1 itself, (b) shows the tap weights w_{12} for compensating inter-channel interference from channel 2. The two channels are assumed symmetrical in ISI and ICI. The data are collected at V_{pp}=600 mV.

Table 1. ISI and ICI measured by LMS tap weights.

Channel/ Code	W_0	RMS ISI	RMS ICI	ISI/W_0	ICI/W_0
NCNS CH1	0.956	0.0755	0.145	7.90%	15.2%
NCNS CH2	0.921	0.0829	0.137	9.00%	14.9%
PAM4 CH1	0.981	0.112	0.195	11.4%	19.8%
PAM4 CH2	0.984	0.112	0.206	11.3%	20.9%

quadrature components and feeds them into the two independent channels in AWG. Simultaneously, an offline file is stored for synchronization. Next, the signal is equalized, amplified and biased for the transmission using LED. The received signal is sampled from the oscilloscope and experiences the inverse process it has been through in the transmitter. An extra step, a least mean square (LMS) software equalization, is added to compensate the linear loss in the channel. To improve the BER performance, LMS algorithm is applied at the receiver. Its taps weights provide evidence to compare the performance of PAM4 and NCNS. Finally, by comparing the decoded information to the original data saved in offline file, the BER is computed and used for evaluation to the communication quality.

The MISO system used in this experiment is built using two LEDs and one PIN photodiode. The LED used is developed by Nanchang University, featuring in 450 nm peak wavelength and maximum 2.25 Gb/s data rate. The PIN is Hamamatsu S10784, of which the usable wavelength covers 400-1000 nm. The oscilloscope is Agilent Technologies MSO9254A and the AWG is SONY Tektronix AWG520. The bias tee and amplifier used in this experiment is Mini-Circuits ZFBT-4R2GW-FT and ZHL-6A-S+.

3. Result

This experiment tests both the PAM4 and NCNS modulation scheme, setting the bias current at 35 mA. The AWG generates the transmitted signal at 900 MSa/s with 3 times upsampling. The data rate in this experiment is therefore 1200 Mbit/s. To demonstrate and compare the strength and weakness of the two modulation schemes, this experiment samples the BER of both at varying V_{pp} from 200 mV to 1000 mV, which includes both the low signal-to-noise case and the high V_{pp} (also high nonlinearity) case. The samples constitute two 5-by-5 grids, whose diagonal line of the shows the case where the two channels are balanced with equal V_{pp} (as the baseline of analysis). The result is plotted in Figure 3. The line chart in Figure 3 shows the case where both channels transmit signal with equal V_{pp}. Although in the low power case below 600 mV V_{pp}, NCNS is outperformed by PAM4, the maximum usable V_{pp} of NCNS is about 100 mV (or 16%) higher than that of PAM4. The insets give more details about this phenomenon. In each group, the three diagrams from left to right indicate the signal quality of PAM4, NCNS, and the result from NCNS decoding, intuitively showing the effect of NCNS.

In 400mV case, because the distance between the constellation points in NCNS is less than that in PAM4, and that SNR is comparatively low, the constellation points in NCNS is less desirable compared with those in PAM4. And so are the constellation points after nonlinear decoding in NCNS. However, the situation is flipped in 600mV case, where the difference in BER is the most significant. The nonlinearity remarkably distorts the PAM4 constellation points, especially the peripheral ones. For example, the constellation points at the four corners are so severely distorted that loss their round shape.

By contrast, NCNS successfully limits the deformation of constellation points. Meanwhile, the decoded result also demonstrates more concentrated constellation points compared with PAM4. The constellation diagram in Figure 3 gives an explanation to the improvement in BER by NCNS, that due to the

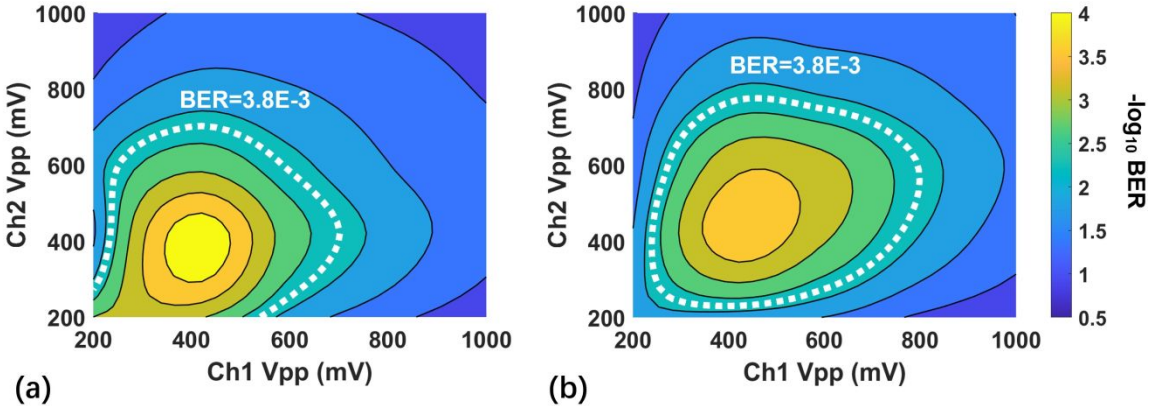

Figure 5. The comparison in averaged BER of the two channels between the (a) PAM4 and (b) NCNS. The area enclosed by the dash line represent the usable area with BER lower than the threshold for 7% forward error coding (FEC). NCNS has 0.24 V^2 dynamic range, which is 33% larger than that of PAM4 (0.18 V^2).

nonuniform distribution, NCNS sends more signal with lower power transmitted and thus avoids the nonlinear region. Although NCNS performs less attractive when the VLC system is SNR restricted, when the nonlinearity replaces noise and becomes the main cause of BER, NCNS performs better than PAM4. This conclusion can be solidified using the Figure 4.

To provide detailed information, the power spectrum at 400 mV and 600 mV V_{pp} are plotted in Figure 4. The histogram of symbols from single channel and after the superposed QAM are also plotted in Figure 4. Compared with PAM4 spectrum in Figure 4(a), the spectrum in 4(e) is less distinguishable from the background noise. However, at 600 mV, with the SNR increased in both spectra in (b) and (f), the signal bands are clearly distinguishable from background noise. 4(c) and 4(g) illustrates the distribution of the received symbols, where PAM4 is mainly uniform while NCNS is otherwise. The last pair of diagrams 4(d) and 4(h) shows the distribution of the superposed QAM signal by PAM4 and by NCNS, which also demonstrates their difference in symbol probability. Furthermore, in Figure 4 (c), the histogram suggests that peaks are overlapping except for the central two, while in 4(g) this phenomenon is less severe. It means that more received symbols are distributed closer to the expected value in NCNS than in PAM4, which means fewer symbols are wrongly decided as it deviates from its original value and falls into the decision region for other symbols.

Assuming the averaged amplitude on each tap of the joint LMS equalizer is the same, the tap weight indirectly gives information about the intensity of ISI and ICI. The result is plotted in Figure 6 , where (a) gives the tap weights w_{11} for ISI and (b) shows tap weights w_{12} for ICI. The RMS value of the tap weights is calculated and recorded in To further explore the details, the RMS value, and the ratio of the center tap weight w_0 to the RMS value of the others are calculated and listed in the Tabel 1, where both channels in NCNS and PAM4 are included. NCNS present a lower ratio in all of the four cases. As the LMS equalizer outputs the weighted sum of all the taps, the squared weight can be interpreted as the influence in signal power from the adjacent symbols, assuming the averaged value from each tap is the same. The central tap (tap 6) in Figure 6 (a) is corresponding to the influence from the expected symbol but the others are regarded as ISI and ICI. The data in table 1 suggests that, in NCNS case, the LMS output is dominant by the expected symbol and less affected by the adjacent one or from the other channel.

The Figure 5 plots two heat maps of the mean BER of the two channels. The result in generated from interpolation to the 5-by-5 grid of the original 25 samples using cubic function. It gives a distinct contrast in dynamic area enclosed by the threshold BER level. The subplot (a) and (b) shows that, NCNS provides a larger dynamic range for a lossless communication with 7% FEC applied, extending the boundary to into the right top corner where the nonlinearity is the most severe. The gradient in color map indicates that NCNS has a flatter BER distribution as the Figure 3 also shows. The dynamic area in NCNS is $2.40 \times 10^5 mV^2$, about 33% larger than that in PAM4($1.8 \times 10^5 mV^2$). The final result in Figure 5 clearly demonstrates the merit of NCNS. Compared with superposed modulation using PAM4, the maximum usable range increases by 33%. This improvement means higher signal power could be applied in VLC system. Meanwhile, the system is more robust against fluctuating V_{pp}. When the bias point is the same, NCNS allows a larger jittering in V_{pp} but still keeps the BER under the threshold.

4. Conclusion

The distribution of symbols plays a decisive role in their performance within the same V_{pp}, which accounts for the most of the difference it presents compared with PAM4. In this experiment, NCNS precoding lowers the averaged signal power and thus increases the dynamic range significantly in high V_{pp}, but sacrifices the systems performance at lower V_{pp}. This feature is desirable in large power VLC system, where the high power frequently causes severe nonlinearity. Apart from terrestrial VLC network, underwater VLC (UVLC) system would be especially benefitted as the power requirement is usually higher to overcome the scattering and absorption. In the meantime, the VLC system could be more robust when jittering presents in V_{pp}. With NCNS and its larger dynamic range, the V_{pp} is less likely to cross the boundary, and thus the VLC system is more possible to control BER under the threshold. This experiment shows that, NCNS-QAM could be a useful modulation scheme in the future and help the VLC system to stretch further and deeper into the unknown region.

Acknowledgement

This work was partially supported by the National Natural Science Foundation of China Project (No.61925104, No.62031011, No. 62074072), the China National Postdoctoral Program for Innovative Talents (BX2021082), China Postdoctoral Science Foundation (2021M700025), and the Major Key Project of PCL (PCL2021A14).

References

[1] Chi, N., Zhou, Y., Wei, Y., & Hu, F. (2020). Visible Light Communication in 6G: Advances, Challenges, and Prospects. IEEE Vehicular Technology Magazine, 15(4), 93-102. https://doi.org/10.1109/MVT.2020.3017153

[2] Jiang, W., Han, B., Habibi, M. A., & Schotten, H. D. (2021). The Road Towards 6G: A Comprehensive Survey. IEEE Open Journal of the Communications Society, 2, 334-366. https://doi.org/10.1109/OJCOMS.2021.3057679

[3] Chen, S., Zhang, J., Jin, Y., & Ai, B. (2020). Wireless powered IoE for 6G: Massive access meets scalable cell-free massive MIMO. China Communications, 17(12), 92-109. https://doi.org/10.23919/JCC.2020.12.007

[4] Lee, Y. L., Qin, D., Wang, L. C., & Sim, G. H. (2021). 6G Massive Radio Access Networks: Key Applications, Requirements and Challenges. IEEE Open Journal of Vehicular Technology, 2, 54-66. https://doi.org/10.1109/OJVT.2020.3044569

[5] Chen, C., Zhong, W., Yang, H., & Du, P. (2018). On the Performance of MIMO-NOMA-Based Visible Light Communication Systems. IEEE Photonics Technology Letters, 30(4), 307-310. https://doi.org/10.1109/LPT.2017.2785964

[6] Wang, W., Zhu, Y., Zhang, Y., & Zhang, J. (2015). An Optimal Power Allocation for Multi-LED Phase-Shifted-Based MISO VLC Systems. IEEE Photonics Technology Letters, 27(22), 2391-2394. https://doi.org/10.1109/LPT.2015.2466573

[7] Ji, H., Qiao, S., & Zhang, T. (2019, 2-5 Aug. 2019). A MISO-VLC System Based on LACO-OFDM and Superposed Constellation Demodulation. 2019 9th International Conference on Information Science and Technology (ICIST)

[8] Qiao, L., Lu, X., Liang, S., Zhang, J., & Chi, N. (2018). MISO visible light communication system utilizing hybrid post-equalizer aided pre-convergence of STBC decoding. Chinese

Optics Letters, 16(6), 060604. https://doi.org/10.1364/COL.16.060604

[9] Wang, C., Li, G., Hu, F., Zhao, Y., Jia, J., Zou, P., Lu, Q., Chen, J., Li, Z., & Chi, N. (2020). Visible light communication for Vehicle to Everything beyond 1 Gb/sbased on an LED car headlight and a 2 × 2 PIN array. Chinese Optics Letters, 18(11), 110602.

[10] Deng, X., Mardanikorani, S., Wu, Y., Arulandu, K., Chen, B., Khalid, A. M., & Linnartz, J. M. G. (2018). Mitigating LED Nonlinearity to Enhance Visible Light Communications. IEEE Transactions on Communications, 66(11), 5593-5607. https://doi.org/10.1109/TCOMM.2018.2858239

[11] Chen, C., Zhong, W., Yang, H., & Du, P. (2018). On the Performance of MIMO-NOMA-Based Visible Light Communication Systems. IEEE Photonics Technology Letters, 30(4), 307-310. https://doi.org/10.1109/LPT.2017.2785964

[12] Zou, P., Liu, Y., Wang, F., & Chi, N. (2018, 26-29 Oct. 2018). Mitigating Nonlinearity Characteristics of Gray-Coding Square 8QAM in Underwater VLC system. 2018 Asia Communications and Photonics Conference (ACP).

[13] Calderbank, A. R., Lee, T., & Mazo, J. E. (1988). Baseband trellis codes with a spectral null at zero. IEEE Transactions on Information Theory, 34(3), 425-434. https://doi.org/10.1109/18.6023

[14] Igarashi, K., Tsuritani, T., & Morita, I. (2016). Polybinary Shaping for Highly-Spectral-Efficient Super-Nyquist WDM QAM Signals. Journal of Lightwave Technology, 34(8), 1724-1731. https://doi.org/10.1109/JLT.2016.2524200

[15] Park, J. S., Gelfand, S. B., & Fitz, M. P. (2010, 31 Oct.-3 Nov. 2010). A spectral shaping nonlinear binary coded modulation with Gray-mapped QAM signals. 2010 - MILCOM 2010 MILITARY COMMUNICATIONS CONFERENCE,

[16] Stojanovic, N., Prodaniuc, C., Karinou, F., & Qiang, Z. (2016, 20-24 March 2016). 56-Gbit/s 4-D PAM-4 TCM transmission evaluation for 400-G data center applications. 2016 Optical Fiber Communications Conference and Exhibition (OFC),

[17] Yamamoto, S., Masuda, A., Taniguchi, H., & Kisaka, Y. (2019, 3-7 March 2019). 92-Gbaud PAM4 Transmission using Spectral-Shaping Trellis-Coded-Modulation with 20-GHz Bandwidth Limitation. 2019 Optical Fiber Communications Conference and Exhibition (OFC),

[18] Yamamoto, S., Taniguchi, H., Matsushita, A., Nakamura, M., Okamoto, S., & Kisaka, Y. (2020). Spectral-Shaping Technique Based on Nonlinear-Coded-Modulation for Short-Reach Optical Transmission. Journal of Lightwave Technology, 38(2), 466-474. https://doi.org/10.1109/JLT.2019.2956189

[19] Buchali, F., Steiner, F., Böcherer, G., Schmalen, L., Schulte, P., & Idler, W. (2016). Rate Adaptation and Reach Increase by Probabilistically Shaped 64-QAM: An Experimental Demonstration. Journal of Lightwave Technology, 34(7), 1599-1609. http://www.osapublishing.org/jlt/abstract.cfm?URI=jlt-34-7-1599

[20] Xin, H., Zhang, K., Kong, D., Zhuge, Q., Fu, Y., Jia, S., Hu, W., & Hu, H. (2019). Nonlinear Tomlinson-Harashima precoding for direct-detected double sideband PAM-4 transmission without dispersion compensation. Optics express, 27(14), 19156-19167. https://doi.org/10.1364/OE.27.019156

[21] Guo, X., & Chi, N. (2020). Superposed 32QAM Constellation Design for 2 × 2 Spatial Multiplexing MIMO VLC Systems. Journal of Lightwave Technology, 38(7), 1702-1711. https://doi.org/10.1109/JLT.2019.2961146

[22] Huang, H., Shih, P., Lin, C., Cheng, Y., Liang, W., Ho, C., Wei, C., & Ng'oma, A. (2014). 2 × 2MIMO OFDM-RoF System Employing LMS-Based Equalizer With I/Q Imbalance Compensation at 60 GHz. IEEE Photonics Journal, 6(3), 1-7. https://doi.org/10.1109/JPHOT.2014.2310222